# Excitation of Mesoscopic Plasmonic Tapers by Relativistic Electrons: Phase Matching *versus* Eigenmode Resonances

Nahid Talebi,*,†,§ Wilfried Sigle,†,§ Ralf Vogelgesang,‡,§ Martin Esmann,‡ Simon F. Becker,‡ Christoph Lienau,‡ and Peter A. van Aken†

†Max Planck Institute for Solid State Research, Heisenbergstr. 1, 70569 Stuttgart, Germany and ‡Institute of Physics and Center of Interface Science, Carl von Ossietzky University, 26129 Oldenburg, Germany. §N.T., W.S., and R.V. contributed equally to this work.

ABSTRACT We investigate the optical modes in three-dimensional single-crystalline gold tapers by means of electron energy-loss spectroscopy. At the very proximity to the apex, a broadband excitation at all photon energies from 0.75 to 2 eV, which is the onset for interband transitions, is detected. At large distances from the apex, though, we observe distinct resonances with energy dispersions roughly proportional to the inverse local radius. The nature of these phenomena is unraveled by finite difference time-domain simulations of the taper and an analytical treatment of the energy loss in fibers. Our calculations and the perfect agreement

with our experimental results demonstrate the importance of phase-matching between electron field and radiative taper modes in mesoscopic structures. The local taper radius at the electron impact location determines the selective excitation of radiative modes with discrete angular momenta.
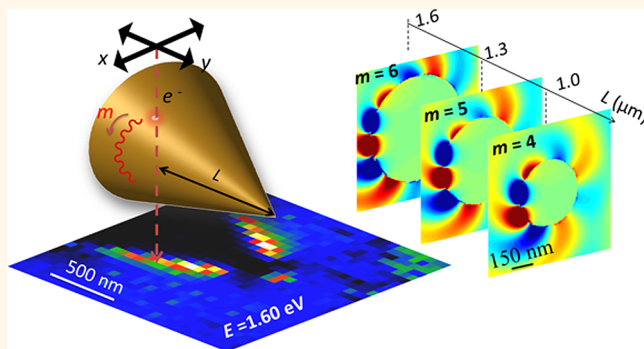
KEYWORDS: photonic local density of states · gold taper · plasmons · electron energy-loss spectroscopy · numerical simulations

Metallic nanostructures are unique nanophotonic functional elements. Their elementary polaritonic excitations, the localized surface plasmon (LSP) modes,[1,2] combine collective oscillations of the metallic electron gas with optical field oscillations. These surface plasmons exhibit light concentration to length scales substantially below the diffraction limit.[3,4] Planar and interface metallic geometries have been extensively studied in the literature for their possibility of supporting the so-called long-range plasmons, either in the form of surface plasmons,[5] channel plasmons,[6] or wedge plasmons.[7,8]

Spectroscopy techniques detecting the energy loss of relativistic electron probes (EELS, electron energy-loss spectroscopy) in electron microscopes were among the pioneering methods to unravel the existence of plasmon oscillations at metal surfaces.[9−13] Since then, these techniques have improved, in both energy and spatial resolution, to become one of the best methods of acquiring plasmon resonances of single metallic

nanostructures.[14−19] EELS has been extensively studied in the literature theoretically and experimentally and is well-known for its ability to unravel the local density of optical states (LDOS)[20] projected along the electron trajectory. However, it is exactly this projection that sets an interesting selection rule for EELS since in inelastic electron scattering the momentum transfer from the electron to the specimen and *vice versa* is huge.[21] Moreover, when the dimension of the specimen along the electron trajectory is mesoscopic rather than nanoscopic, a dynamic interchange of momentum and energy between the electron and specimen can take place, as will be shown here.

Using EELS, we study three-dimensional single-crystalline gold tapers. These tapers have demonstrated the ability of nanolocalizing the optical density of states at the apex by effectively coupling the surface plasmons along the shaft to the localized plasmons of the apex.[22−24] Indeed, efficient coupling and nanolocalization is possible only by the presence of the proper optical

modes that the gold taper sustains. These modes provide a smooth and diffraction-free transfer of the energy to its rotationally symmetric fundamental mode at the apex.[25] Here, we study the coupling of swift electrons to the optical modes of the taper and its implications for the nanofocusing of surface plasmons.

We selectively choose a gold taper with an extreme change in the local radius of the cross section, from the very nanometer scale at the apex toward the meso-scopic scale along the shaft. We show that this dimen-sional aspect reveals an interesting selection rule for the electron−plasmon inelastic interaction. While at the very apex we can excite the rotationally symmetric optical mode with an extremely broad bandwidth, this mode is not efficiently excited along the shaft for a gold taper with a large opening angle. Rather, we detect the radiative modes of the gold taper along the shaft. Intriguingly, the excited modes dynamically interact with the swift electron in such a way that an interference pattern emerges in the EELS map, display-ing energy *versus* impact parameter. We underpin our interpretation by analytical calculations of the EEL spectra. We compare the data with the analytically calculated EELS of gold fibers. Considering all the observations, we propose a simple model for under-standing the dispersion of the higher-order resonances we observe in EEL spectra by imposing a phase-matching criterion.

RESULTS

We use single-crystalline gold tapers, whose particu-larly smooth surfaces eliminate surface plasmon polar-iton (SPP) localization[26] and scattering losses along the taper shaft. Figure 1a shows a dark-field transmission electron microscope image of a taper with an opening angle of $\alpha = 49°$. Experimental and simulation results for a gold taper with a smaller opening angle of 19° are also shown in the Supporting Information.

EELS and energy-filtered transmission electron microscopy (EFTEM) experiments were conducted at the Zeiss SESAM microscope[27] operated at an accelera-tion voltage of 200 kV.

The EELS signal reflects the probability of the elec-tron beam to excite surface plasmons during the interaction with the sample and thus senses the LDOS projected onto the trajectory of the electron.[20] EELS allows measuring this LDOS from a few tens of milli-electronvolts to hundreds of electronvolts and thus is ideally suited for probing ultra-broad-band excitations. Figure 1b shows images at selected energy losses extracted from a series of EEL spectra with a spatial resolution of just 50 nm. Already, these overview maps exhibit a spatially well-localized energy-loss signal at the taper apex for energy losses below 2 eV. At higher energies, interband absorption in gold sets in,[28] resulting in a spatially homogeneous EELS signal in the vicinity of the metal surface. At lower energy losses
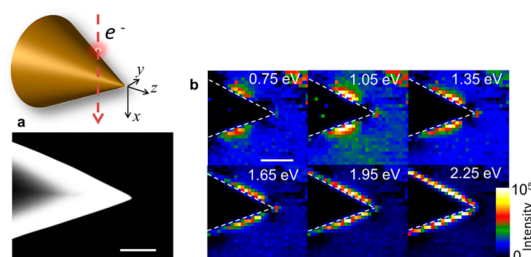
Figure 1. (a) Dark-field transmission electron microscopy image of a taper with an opening angle of $\alpha = 49°$; the above inset shows the three-dimensional topology of the taper. **(b)** Images of the electron energy-loss intensity at six selected energy losses between 0.75 and 2.25 eV. These data are extracted from a series of 30×28 EEL spectra that were recorded at electron impact locations on a rectangular grid with a pixel size of 50 nm. The color scales of the images are given in linear arbitrary units. Scale bar lengths are 500 nm.
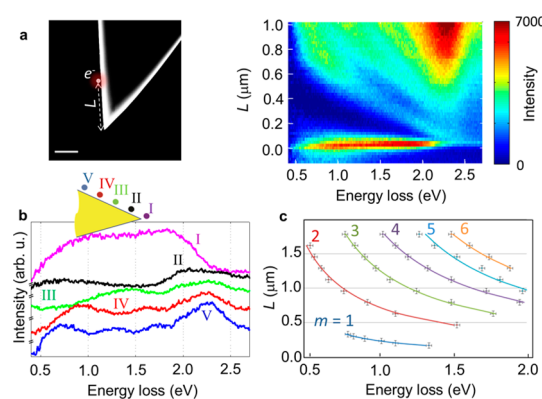
Figure 2. Imaging and spectroscopy of a gold taper with an opening angle of $\alpha = 49°$. **(a)** Zero-loss-corrected electron energy-loss intensity as a function of impact location along the taper shaft. At certain distances, L, between electron impact and taper apex, pronounced resonance peaks are revealed. The length of the scale bar is 1 μm. **(b)** EELS for electron impact at the apex (purple) and at distances of 276 nm (black), 506 nm (green), 736 nm (red), and 966 nm (blue) from the apex. The spectra are shifted vertically for clarity. The zero-loss peak contribution was subtracted from the individual spectra by using a power-law fit. **(c)** Disper-sions of maxima in EEL spectra *versus* the distance from the taper. These maxima are denoted by their corresponding mode numbers ($m = 1, 2, …$). Curves are least-squares fits to a hyperbolic function $E = E_0 + \kappa/L$, where κ and E_0 are constants.

($E = 0.75$ to 1.35 eV), we find an additional pronounced EELS signature as bright lobes penetrating from the shaft surface into the vacuum. These lobes are con-fined to a region of a few hundred nanometers along the shaft and are markedly displaced from the apex. As discussed below, this can be related to taper eigenmodes with higher-order angular momentum. The broad-band ability of those tapers to localize light in exceedingly small volumes at the apex is seen in a series of EEL spectra recorded at various positions along the shaft (Figure 2b) for a gold taper with the opening angle of 49°. Near the apex, an intense, spatially localized and spectrally broad-band EELS signal emerges, reflect-ing the confined LSPs at the taper apex. Interestingly,

its intensity remains almost constant within the range from ~0.75 eV, a lower limit imposed by the difficulty of subtracting the zero-loss peak, to ~2.0 eV, the onset of interband absorption. As such, the bandwidth of this resonance covers more than one octave, in distinct contrast to the spectrally narrower LSP resonances of metallic nanoparticles and also to earlier EELS measurements on conical tapers of finite length.[29]

When moving the electron excitation away from the apex, the EELS signal vanishes entirely, until, at a finite distance from the apex, a second contribution sets in, leading to a sequence of distinct maxima in the energy-loss spectra (Figure 2b) at energy losses below 2 eV. The spectral width of these resonances is in the range of a few hundred millielectronvolts. As displayed in Figure 2c, for each individual resonance in this sequence, the dispersion is well represented by a hyperbolic function of the form $E = E_0 + \kappa/L$, with $L = R/\sin(\alpha/2)$ being the distance from the apex and R being the local radius. Remarkably, the fitting parameters depend on the sequence number m in a linear fashion, resulting in the empirical relation

$$E = (0.105m - 0.098)\,\text{eV} + \frac{(0.139m - 0.014)}{R}\,\mu\text{m}\cdot\text{eV} \quad (1)$$

As will be shown below, this resonance behavior is a consequence of phase-matching between the exciting electron and the local taper mode fields. The parameter m is directly related with the angular momentum of eigenmodes with higher-order azimuthal symmetry.

Numerical Results. In order to understand the physics behind our experimental observations, we have to consider the whole set of possible eigenmodes of the system. Scattering by conical structures has been studied in numerous works for decades.[30,31] Explicit solutions are still the subject of ongoing research, involving rather advanced applications of integral transforms[32] or novel approximation methods based on quasi-separation of variables.[33] Here, we adopt the more intuitive stance of viewing the metallic cone as a three-dimensional taper formed from metallic fiber segments of infinitesimal height. Particularly, the local near-field behavior of taper eigenmodes can be described effectively by a superposition of the eigenmodes of fibers with continuously varying radii. The fiber eigenmodes are calculated by solving the Helmholtz equation in a cylindrical coordinate system.[34,35] They are characterized by the complex wavenumber k_z along the fiber axis and the azimuthal angular momentum number $m = 0, \pm 1, \pm 2, \dots$. The mode field outside the fiber can thus be derived from a potential of the form (see also Supporting Information)

$$\Phi_{m,k_z,\omega}(x,y,z,t) \propto H_m^{(1)}(k_\rho\rho)e^{ik_z z}e^{im\phi}e^{-i\omega t} + cc \quad (2)$$

where $H_m^{(1)}$ is the Hankel function of first kind, $(\rho\cos\phi, \rho\sin\phi) = (x,y)$, $k_\rho^2 = k_0^2 - k_z^2$, and $\omega = c_0 k_0$ is the angular

frequency of the mode. It is well-known that only the fundamental $m = 0$ mode of a metallic taper is evanescently bound to the surface regardless of local radius.[36,37] It propagates to the apex with high efficiency and with a concomitant increase in the effective refractive index and hence the localization of light.[22,38] This process requires a smooth transition of the local radius of the taper. In addition to the propagating $m = 0$ mode, there are higher-order modes, characterized by $|m| \geq 1$, which may also propagate with low loss toward the apex as bound modes, at least where the local radius is larger than a mode-specific critical value. At the critical radii, however, they couple to the radiative (unbound) continuum of photonic modes. For instance, on a gold taper excited at a vacuum wavelength of 800 nm, the critical radii of the $|m| = 1$ and $|m| = 2$ mode are approximately $R \approx 100$ nm and $R \approx 600$ nm, respectively.[25] It should be noted that, in addition to the modes mentioned above, for any given parameter pair $\{m,\omega\}$, there exists a continuum of discrete values in the complex k_z plane that satisfy the eigenmode equation. They are characterized by rapidly increasing imaginary parts, and the corresponding modes may contribute to an acute localization along the taper shaft but decay quickly upon propagation. That is because they sustain oscillatory amplitude inside the core along the radial direction, though evanescent in the air region. In order to understand if and how these features of a local fiber description of a plasmonic taper may be used to explain the experimentally observed EELS results, we discuss in the following the first numerical simulations of the electron energy-loss process near three-dimensional taper structures. These and the experimental results are then compared to an analytical model for EELS near fibers, which allow a detailed discussion of the individual contributions of different k_z and m components.

We perform numerical finite-difference time-domain (FDTD) calculations of three-dimensional tapers with an embedded relativistic electron source.[39−41] The electron is assumed to pass the taper on a straight line 1 nm from its surface. The speed of $V \approx 0.695c_0$ is chosen (unless specified otherwise) in correspondence with the acceleration voltage of 200 kV used in the experiments. Figure 3a displays an instantaneous distribution of the $E_z(\vec{r},t)$ field component on the taper surface at a moment about 1 fs before the electron approaches closest to the taper, about 900 nm from the apex. Further time frames from the same simulation are shown in Figure 3c for cross sections normal to the taper axis. Full movies of the entire interaction time are available in the Supporting Information. An analysis of the spatial and temporal evolution of the fields in such simulations reveals two main features. First, a wave packet of radiation emerges from the interaction volume as an almost spherical, ultrashort light pulse, propagating away freely from the electron at approximately vacuum speed of light. Second, a comparatively
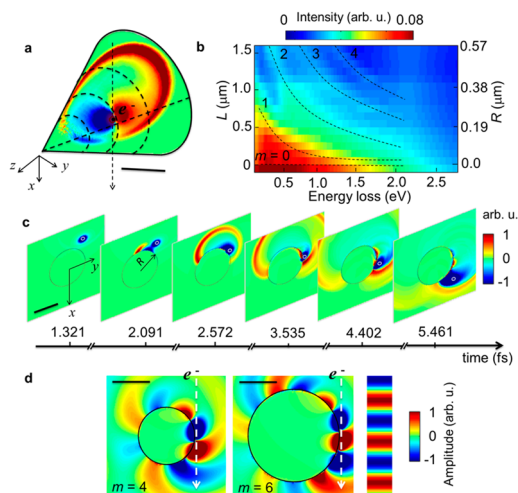
Figure 3. Dynamical simulation of the energy loss of relativistic electrons upon passing a gold taper with an opening angle of $\alpha = 45°$. The taper axis is denoted as z, and the electron trajectory is assumed to be parallel to the x axis. (a) Snapshot of the instantaneous component E_z of the total electric field at the surface of the taper for an electron impacting just outside the surface at a distance of $L = 900$ nm from the apex, corresponding to a local radius of $R = 344$ nm. (b) Computed EEL spectra as a function of energy loss and impact location along the taper shaft. The dashed lines are guides for the eyes. (c) Series of instantaneous total electric field distribution for several times during the passage of the electrons by the taper at $L = 900$ nm. The panels show $E_z(x,y,t)$ in an xy plane located $\delta z = 5$ nm behind the electron trajectory. (d) Maps of the scattered electric field component, E_z, at an energy loss of 1.6 eV for electron impact at distances of $L = 1$ μm (left, $R = 383$ nm) and $L = 1.6$ μm (middle, $R = 612$ nm) from the taper apex. The right panel shows the plane wave component $k_x = \omega/V = 11.7$ rad/μm ($2\pi/k_x = 539$ nm) of the electric field associated with the relativistic electron, which corresponds to an energy of 1.6 eV. Scale bars are 500 nm.

minor part of the transferred energy is converted into evanescent surface modes that continue to propagate along the z axis. Evidently, the electron impulsively launches a wave packet composed of modes in a very broad energy range, with a wide distribution of azimuthal orders m and wavenumbers k_z along the taper axis. For the local radius of $R = 344$ nm at the electron impact, only fiber modes with $m = 0$ and $|m| = 1$ exhibit (locally) bound character and may propagate along the taper shaft. Other modes are either unbound (contributing to the free light pulse) or strongly evanescent along the taper shaft as well as normal to the surface. The full distribution of the evanescent and radiative modes at each local radius of the taper is discussed below.

In Figure 3b, calculated EEL spectra are shown for different distances L from the taper apex. Clear signatures of discrete resonances emerge, in full accord with the experimental findings displayed in Figure 2a. At this point, however, the time domain calculations by themselves offer little further insight into the characteristic hyperbolic dispersions of EELS probability maxima as functions of the local taper radius.

We have therefore developed an analytical description of the electron energy-loss mechanism for infinitely long fibers (see Supporting Information). When the energy-loss probability is expanded into a sum over mode order m and Fourier-analyzed in both the k_z and the ω domain, we find the partial probability is represented by

$$\Gamma_m^{EELS}(k_z, \omega) = \left(\frac{-q}{\pi\hbar\omega}\right)\mathscr{R}i^m\frac{k_\rho}{2}e^{-im\phi_e}e^{ik_yy_0}$$
$$\times \{(-\frac{k_z}{\omega\varepsilon_0}C_{A,m}^{D_2}(k_z,\omega) - iC_{F,m}^{D_2}(k_z,\omega))\int_{-\infty}^{+\infty}dx e^{-i\frac{\omega}{V}x}H_{m-1}^{(1)}(k_\rho\rho)e^{i(m-1)\phi}$$
$$+ (\frac{k_z}{\omega\varepsilon_0}C_{A,m}^{D_2}(k_z,\omega) - iC_{F,m}^{D_2}(k_z,\omega))\int_{-\infty}^{+\infty}dx e^{-i\frac{\omega}{V}x}H_{m+1}^{(1)}(k_\rho\rho)e^{i(m+1)\phi}\}$$
$$(3)$$

Here, ε_0 is the vacuum dielectric constant and $q = -e_0$ is the electron's charge. Abbreviating $k_x = \omega/V$, the wave vector of the electromagnetic field, which is associated with the moving electron, is described in the xy plane with $k_\rho^2 = k_0^2 - k_z^2 = k_x^2 + k_y^2$ and $\tan\varphi_e = -k_y/k_x$. The coefficient functions $C_{A,m}^{D_2}(k_z,\omega)$ and $C_{F,m}^{D_2}(k_z,\omega)$ represent the amplitudes of the electromagnetic fields scattered by the fiber.

Equation 3 provides an instructive distinction between two very different mechanisms of obtaining resonant EELS signals. The first factors are the scattering coefficients. Notably, all four coefficient functions share the common resonance denominator (see Supporting Information)

$$\Delta = \left(\frac{k_\rho}{k_\rho^{D_1}}\right)^2(k_\rho H_m^{(1)}J_m{}' - k_\rho^{D_1}H_m^{(1)'}J_m)(\varepsilon_r k_\rho H_m^{(1)}J_m{}'$$
$$- k_\rho^{D_1}H_m^{(1)'}J_m) - \left[\left(\left(\frac{k_\rho}{k_\rho^{D_1}}\right)^2 - 1\right)\frac{m}{a}\frac{k_z}{k_0}H_m^{(1)}J_m\right]^2 \quad (4)$$

The vanishing of this term is precisely the condition for the eigenmodes of fibers.[34,35] That is, whenever the excitation due to the swift electron is such that the field scattered by the fiber closely resembles an eigenmode, the divergence of the scattering coefficients implies a strong EELS signal.

A second curious feature of the fully expanded EELS probability, $\Gamma_m^{EELS}(k_z,\omega)$, is the integrals that are evaluated along the electron trajectory, $\vec{r}(x) = (x,y_0,0) = (\rho\cos(\phi), \rho\sin(\phi), 0)$. They have the form of an overlap integral

$$\int_{-\infty}^{+\infty}dx[e^{-i\omega x/V}] \times [H_{m\pm1}^{(1)}(k_\rho\rho)e^{i(m\pm1)\phi}] \quad (5)$$

with factors resembling the spatial part $\exp(-i\omega x/V)$ of the Fourier component of the electron field at frequency ω and that of fiber eigenmodes (cf. eq 2). Thus, a resonant transfer of energy from the electron to the plasmonic structure can be expected whenever these two factors exhibit a closely matching spatial phase pattern. This is indeed what we observe in the FDTD calculations, as Figure 3d shows. For a fixed frequency $\omega = 1.6$ eV/$\hbar$, the electron field oscillates along the trajectory with a constant wavelength of about 539 nm

(right panel). Fourier transforms of the FDTD results to the frequency domain, evaluated for the same frequency ω, show that the scattered fields are particularly strong only when the electron passes the taper at specific local radii (left two panels). The field distributions, in turn, resemble the mode field patterns of individual fiber modes (here for $m = 4$ and $m = 6$), but not exactly, since the interaction of the electron with the taper involves a multitude of eigenmodes.

An approximate selection rule for observing phase-matching resonance in EELS of fibers follows from finding a condition for which the overlap integral (eq 5) attains maximal values. A crude estimate is obtained if the integral is evaluated only over a certain "interaction length", where the integrand attains its largest magnitude, that is, close to the fiber. This truncated interval becomes maximal when the phases of the electron field and the fiber mode field match over the interaction length. The (unrealistic) assumption that the interaction length extends only over small angles $\phi = \arctan (x/y_0) \approx x/R$ leads to the condition

$$\hbar\omega \approx (m \pm 1)\frac{\hbar V}{R} \qquad (6)$$

In comparing this to the empirical result from Figure 2a, eq 1, we find that this expression already captures the qualitative features quite well. The hyperbolic functional relation between the resonance energy and the local radius is found with a scaling factor of $\hbar V = 0.137\ \mu\text{m} \cdot \text{eV}$, which is remarkably close to the empirical value of $0.139\ \mu\text{m} \cdot \text{eV}$. As in the experiment, we find equidistant energy spacing between successive resonances at a given local radius. Nevertheless, a quantitative agreement with the experimental data is not achieved by this simplistic phase-matching condition, indicating the need for a more extensive analytical treatment of eq 5 for much longer interaction lengths.

DISCUSSION

Whereas in EELS experiments the loss probability is dispersed only into its energy spectrum, eq 3 affords us with the opportunity of expanding it further into its angular momentum about the fiber axis and the linear momentum along the fiber axis. Figure 4b shows a momentum-resolved EELS (MREELS) map, calculated for a gold fiber with a small radius of $R = 50$ nm and summed over all the m orders. Figure 4c shows individual MREELS maps for angular mode orders $m = 0$ and $m = 1$. Evidently, the rotationally symmetric $m = 0$ mode is the dominant contribution to the sum. The solutions to the characteristic eq 4 are shown by the dashed line in the figure panel. In fact, the $m = 1$ mode contributes strongly only at energies above 2.0 eV, where the volume plasmon in gold is excited. The EELS signal of this comparatively thin fiber closely resembles the $m = 0$ eigenmode dispersion with a narrow spectral width of less than 100 meV. It is due mainly to the
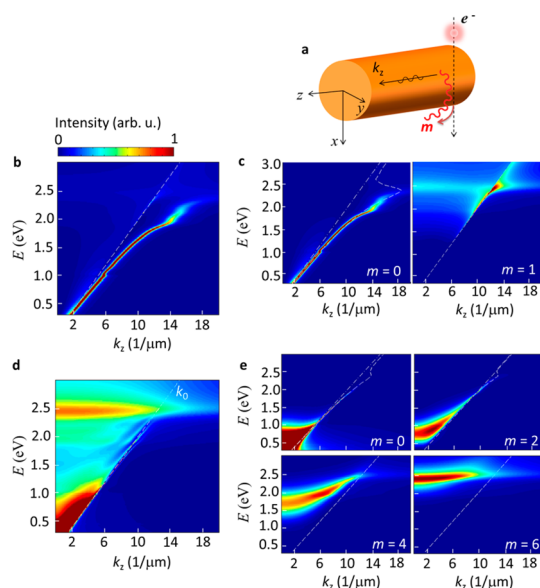
Figure 4. (a) Swift electron interacting with a metallic fiber can excite both evanescent SPP modes that propagate along the fiber as well as radiative modes of the fibers with different angular momentum numbers. The color scale was normalized individually for each panel. Calculated MREELS maps *versus* the linear momentum along the axis of a gold fiber, (b) for a fiber radius of $R = 50$ nm summed over all the angular momentum contributions, (c) for the individual excited angular momentum orders $m = 0$ and $m = 1$, (d) for a fiber radius of $R = 400$ nm summed over all the angular momentum contributions, and (e) for individual excited angular momentum orders $m = 0, 2, 4, 6$ as indicated in each panel. The straight dashed lines indicate the light line ($E = \hbar c_0 k_z$) and the dashed curves $m = 0$ (b) and $m = 0, 2$ (d) are traces of the corresponding fiber eigenmodes dispersions, $\mathcal{R}(k_z(E))$.

resonant denominator of eq 4. Phase-matching resonances according to eq 5 are not relevant.

However, this situation changes drastically when the gold fiber has a larger radius, which increases the effective "interaction length". In Figure 4d, the calculated MREELS map is shown for a fiber of radius $R = 400$ nm. Somewhat surprisingly, these are the radiative modes—characterized by $k_z < k_0$, where $k_0 = E/\hbar c$ is the vacuum wavenumber of light—that dominate the total EELS signal. Significant contributions due to the bulk plasmon are observed again for energies above 2.0 eV, and the evanescent contributions (for $k_z > k_0$) are negligible in comparison, with only faint hints of fiber eigenmode resonances for lower values of $|m|$. The EEL spectra for individual angular momentum orders, as shown in Figure 4e, unravel the physics behind the experimentally observed resonances in the EEL spectra. In fact, the radiative part of the EEL spectra at each momentum contribution exhibits a clear peak *versus* energy, the position of which depends on m. The spectral width of these resonances of a few hundred millielectronvolts is in accord with that of the experimentally observed resonances. Consequently, for such larger radii, the EELS signal is mostly influenced by the spatial phase-matching along the electron trajectory, much less by resonances due to excitation of fiber eigenmodes.
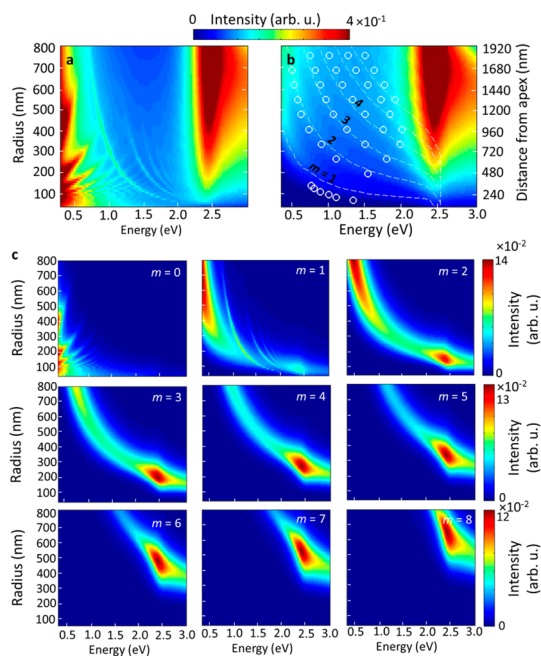
Figure 5. Computed electron energy-loss probability as a function of energy loss and fiber radii, (a) including and (b) excluding the contribution of the *evanescent* modes with $k_z > k_0$. The electron is traveling at a distance of 1 nm from the surface. Experimental data are depicted with solid circles. The dashed lines track the maximum EELS signal according to eq 3 for given radius and mode order. (c) Computed EEL spectra from each angular momentum order.

To further underpin our interpretation, we have calculated the EEL spectra for increasing fiber radius, from $R = 40$ nm to $R = 800$ nm, thus representing the taper in the local radius approximation. Figure 5a shows the total computed EELS intensity, summed over m and integrated over k_z. At low energy loss, we find that bound eigenmodes of the fiber are very dominant. Experimentally, though, we do not observe sharp fibermode-like resonance dispersions because the taper with its opening angle of 49° deviates too strongly from the geometry of fibers. Tapers with a much shallower opening angle (below 10°) would be required for that. Indeed, a taper with an opening angle of 49° cannot support the fiber eigenmodes with $m > 0$ since such modes will couple strongly to the radiation continuum. The resulting map of energy-loss probability *versus* energy and local radius is displayed in Figure 5b. Its resemblance with the experimental data from Figure 2 is striking. For a one-to-one comparison, circles mark selected experimentally observed resonance maxima in Figure 5b. This is a strong indication that the nearly hyperbolically dispersed resonance maxima are due to phase-matching over extended parts of the electron trajectory, as suggested by the overlap integral (eq 5).

A final proof of this conclusion is presented in Figure 5c, where individual panels for azimuthal orders $m = 0-8$ are shown. Clearly, each of the observed resonance dispersions is associated with a different order.

CONCLUSION

In summary, EELS maps were recorded along the shaft of conical gold tapers. At the apex, these confirm the ultra-broad-band ability of such tapers to concentrate light into nanometric volumes. At remote locations along the shaft, surprising resonance dispersions are found. All these observations are confirmed by FDTD calculations. For deeper insight into their nature, we adopt the framework of viewing the taper as composed of infinitesimal fiber segments and develop an analytical expression for the EELS signal from fibers. Besides the possibility of exciting eigenmodes, a phase-matching condition is identified, which also results in the emergence of resonance maxima. In the application of this analysis, we identify the scattering of radiative modes as being responsible for the observed resonance dispersions. Our results thus verify the excitation of modes with certain angular momentum orders, placing emphasis on the crucial role phase-matching plays in the interpretation of EELS data.

It should be noted that reflection from the apex can also modulate the EELS signal due to the formation of a standing wave along the taper shaft. However, as apparent from the movies provided as Supporting Information, the contribution of the reflection from the apex is much weaker than the contribution of the radiative modes and has minor importance under our experimental conditions.

Our findings highlight an important caveat to the well-known intimate relation between EELS probabilities and the projected LDOS near a specimen under study. Strictly, these two quantities are proportional only for structures that are translationally invariant (or periodic) along the electron trajectory.[20] Also, in thin planar sample geometries, the EELS probability closely mimics the LDOS of the structure. Generally, though, for finite sample structures with dimensions along the electron trajectory that are larger than the inverse wavenumber $1/k_x = V/\omega$ of the electromagnetic fields of the electron along this direction, phase-matching must be taken into consideration, and results do depend on the electron speed. Moreover, specific electron velocities are required to couple with radiative modes with $m > 1$ in mesoscopic metallic fibers, tapers, and spheres; specifically, electrons at energies lower than 100 keV cannot detect the kind of phase-matching-related resonances observed in the present study.

METHODS

Sample Preparation. Single-crystalline gold tapers have been produced using the method described previously.[24]

Polycrystalline gold wires with a diameter of 125 μm were annealed at 800 °C for 8 h. The wires were then electrochemically etched in hydrochloric acid (aq. 37%). Rectangular voltage

pulses with a frequency of 3 kHz and a duty cycle of 10% were applied between the wire and a platinum ring, serving as the counter electrode.

EELS. EELS and energy-filtered transmission electron microscopy (EFTEM) experiments were conducted at the Zeiss SESAM microscope[27] operated at an acceleration voltage of 200 kV. The microscope is equipped with an electron monochromator (CEOS Heidelberg) and the MANDOLINE energy filter. EELS data were acquired with an energy resolution of 90 meV as determined from the full width at half-maximum of the zero-loss peak (ZLP). The acquisition time was 0.2 s per spectrum, and the energy dispersion was 4.5 meV/pixel. The energy-loss spectrum was dispersed perpendicular to the energy-dispersive direction on the CCD camera in order to make the full dynamic range of almost 1000 between ZLP and plasmonic peaks accessible without saturating the camera.

FDTD Simulations. In order to perform the FDTD simulations with electron probes, a charge broadening scheme has been introduced, as described previously.[39,41] The whole simulation domain has been discretized by unit cells of 5 nm edge lengths. The permittivity of the gold taper is modeled by a Drude model in addition to two other critical functions that effectively model the interband transition[28] and perfectly matches the experimental data within the energy range of 0.4−3 eV.

Conflict of Interest: The authors declare no competing financial interest.

Supporting Information Available: Simulation movies for a swift electron interaction with gold taper. Different field components are captured over the surface of the taper and normal to the taper axis. Derivation of analytical EELS spectra for fibers. The Supporting Information is available free of charge on the ACS Publications website at DOI: 10.1021/acsnano.5b03024.

REFERENCES AND NOTES

1. Quinten, M.; Leitner, A.; Krenn, J. R.; Aussenegg, F. R. Electromagnetic Energy Transport *via* Linear Chains of Silver Nanoparticles. *Opt. Lett.* **1998**, *23*, 1331–1333. DOI: 10.1364/OL.23.001331.

2. Talebi, N.; Mahjoubfar, A.; Shahabadi, M. Plasmonic Ring Resonator. *J. Opt. Soc. Am. B* **2008**, *25*, 2116–2122. DOI: 10.1364/JOSAB.25.002116.

3. Gramotnev, D. K.; Bozhevolnyi, S. I. Nanofocusing of Electromagnetic Radiation. *Nat. Photonics* **2013**, *8*, 13–22. DOI: 10.1038/nphoton.2013.232.

4. Novotny, L.; van Hulst, N. Antennas for Light. *Nat. Photonics* **2011**, *5*, 83–90. DOI: 10.1038/nphoton.2010.237.

5. Berini, P. Long-Range Surface Plasmon Polaritons. *Adv. Opt. Photonics* **2009**, *1*, 484–588. DOI: 10.1364/AOP.1.000484.

6. Bozhevolnyi, S. I.; Volkov, V. S.; Devaux, E.; Laluet, J. Y.; Ebbesen, T. W. Channel Plasmon Subwavelength Waveguide Components Including Interferometers and Ring Resonators. *Nature* **2006**, *440*, 508–511. DOI: 10.1038/nature04594.

7. Bian, Y. S.; Zheng, Z.; Liu, Y.; Liu, J. S.; Zhu, J. S.; Zhou, T. Hybrid Wedge Plasmon Polariton Waveguide with Good Fabrication-Error-Tolerance for Ultra-Deep-Subwavelength Mode Confinement. *Opt. Express* **2011**, *19*, 22417–22422. DOI: 10.1364/OE.19.022417.

8. Gu, L.; Sigle, W.; Koch, C. T.; Ögüt, B.; van Aken, P. A.; Talebi, N.; Vogelgesang, R.; Mu, J.; Wen, X.; Mao, J.

9. Ritchie, R. H. Plasma Losses by Fast Electrons in Thin Films. *Phys. Rev.* **1957**, *106*, 874–881. DOI: 10.1103/PhysRev.106.874.

10. Pines, D.; Bohm, D. A Collective Description of Electron Interactions 0.2. Collective *vs* Individual Particle Aspects of the Interactions. *Phys. Rev.* **1952**, *85*, 338–353. DOI: 10.1103/PhysRev.85.338.

11. Powell, C. J.; Swan, J. B. Origin of the Characteristic Electron Energy Losses in Magnesium. *Phys. Rev.* **1959**, *116*, 81–83. DOI: 10.1103/PhysRev.116.81.

12. Powell, C. J.; Swan, J. B. Origin of the Characteristic Electron Energy Losses in Aluminum. *Phys. Rev.* **1959**, *115*, 869–875. DOI: 10.1103/PhysRev.115.869.

13. Ritchie, R. H.; Howie, A. Inelastic-Scattering Probabilities in Scanning-Transmission Electron-Microscopy. *Philos. Mag. A* **1988**, *58*, 753–767. DOI: 10.1080/01418618808209951.

14. Garcia de Abajo, F. J. Optical Excitations in Electron Microscopy. *Rev. Mod. Phys.* **2010**, *82*, 209–275. DOI: 10.1103/RevModPhys.82.209.

15. Nelayah, J.; Kociak, M.; Stephan, O.; Garcia de Abajo, F. J.; Tence, M.; Henrard, L.; Taverna, D.; Pastoriza-Santos, I.; Liz-Marzan, L. M.; Colliex, C. Mapping Surface Plasmons on a Single Metallic Nanoparticle. *Nat. Phys.* **2007**, *3*, 348–353. DOI: 10.1038/nphys575.

16. Chu, M.; Myroshnychenko, V.; Chen, C. H.; Deng, J.; Mou, C. Y.; Garcia de Abajo, F. J. Probing Bright and Dark Surface-Plasmon Modes in Individual and Coupled Noble Metal Nanoparticles Using an Electron Beam. *Nano Lett.* **2009**, *9*, 399–404. DOI: 10.1021/nl803270x.

17. Alber, I.; Sigle, W.; Müller, S.; Neumann, R.; Picht, O.; Rauber, M.; van Aken, P. A.; Toimil-Molares, M. E. Visualization of Multipolar Longitudinal and Transversal Surface Plasmon Modes in Nanowire Dimers. *ACS Nano* **2011**, *5*, 9845–9853. DOI: 10.1021/nn2035044.

18. Garcia de Abajo, F. J. Nonlocal Effects in the Plasmons of Strongly Interacting Nanoparticles, Dimers, and Waveguides. *J. Phys. Chem. C* **2008**, *112*, 17983–17987. DOI: 10.1021/jp807345h.

19. Aizpurua, J.; Rivacoba, A. Nonlocal Effects in the Plasmons of Nanowires and Nanocavities Excited by Fast Electron Beams. *Phys. Rev. B: Condens. Matter Mater. Phys.* **2008**, *78*, 035404. DOI: 10.1103/PhysRevB.78.035404.

20. García de Abajo, F. J.; Kociak, M. Probing the Photonic Local Density of States with Electron Energy Loss Spectroscopy. *Phys. Rev. Lett.* **2008**, *100*, 106804. DOI: 10.1103/PhysRevLett.100.106804.

21. García de Abajo, F. J.; Rivacoba, A.; Zabala, N.; Yamamoto, N. Boundary Effects in Cherenkov Radiation. *Phys. Rev. B: Condens. Matter Mater. Phys.* **2004**, *69*, 155420. DOI: 10.1103/PhysRevB.69.155420.

22. Stockman, M. I. Nanofocusing of Optical Energy in Tapered Plasmonic Waveguides. *Phys. Rev. Lett.* **2004**, *93*, 137404. DOI: 10.1103/PhysRevLett.93.137404.

23. Ropers, C.; Neacsu, C. C.; Elsaesser, T.; Albrecht, M.; Raschke, M. B.; Lienau, C. Grating-Coupling of Surface Plasmons onto Metallic Tips: A Nanoconfined Light Source. *Nano Lett.* **2007**, *7*, 2784–2788. DOI: 10.1021/nl071340m.

24. Schmidt, S.; Piglosiewicz, B.; Sadiq, D.; Shirdel, J.; Lee, J. S.; Vasa, P.; Park, N.; Kim, D. S.; Lienau, C. Adiabatic Nanofocusing on Ultrasmooth Single-Crystalline Gold Tapers Creates a 10-nm-Sized Light Source with Few-Cycle Time Resolution. *ACS Nano* **2012**, *6*, 6040–6048. DOI: 10.1021/nn301121h.

25. Esmann, M.; Becker, S. F.; da Cunha, B. B.; Brauer, J. H.; Vogelgesang, R.; Gross, P.; Lienau, C. K-Space Imaging of The Eigenmodes on a Sharp Gold Taper for Near-Field Scanning Optical Microscopy. *Beilstein J. Nanotechnol.* **2013**, *4*, 603–610. DOI: 10.3762/bjnano.4.67.

26. Gresillon, S.; Aigouy, L.; Boccara, A. C.; Rivoal, J. C.; Quelin, X.; Desmarest, C.; Gadenne, P.; Shubin, V. A.; Sarychev, A. K.; Shalaev, V. M. Experimental Observation of Localized Optical Excitations in Random Metal-Dielectric Films.

Resonant Wedge-Plasmon Modes in Single-Crystalline Gold Nanoplatelets. *Phys. Rev. B: Condens. Matter Mater. Phys.* **2011**, *83*, 195433. DOI: 10.1103/PhysRevB.83.195433.

Phys. Rev. Lett. **1999**, *82*, 4520–4523. DOI: 10.1103/PhysRevLett.82.4520.

27. Koch, C. T.; Sigle, W.; Hoschen, R.; Ruhle, M.; Essers, E.; Benner, G.; Matijevic, M. SESAM: Exploring the Frontiers of Electron Microscopy. *Microsc. Microanal.* **2006**, *12*, 506–514. DOI: 10.1017/S1431927606060624.

28. Etchegoin, P. G.; Le Ru, E. C.; Meyer, M. An Analytic Model for the Optical Properties of Gold. *J. Chem. Phys.* **2006**, *125*, 164705. DOI: 10.1063/1.2360270.

29. Huth, F.; Chuvilin, A.; Schnell, M.; Amenabar, I.; Krutokhvostov, R.; Lopatin, S.; Hillenbrand, R. Resonant Antenna Probes for Tip-Enhanced Infrared Near-Field Microscopy. *Nano Lett.* **2013**, *13*, 1065–1072. DOI: 10.1021/nl304289g.

30. Felsen, L. B.; Marcuvitz, N. *Radiation and Scattering of Waves*; Prentice Hall: Englewood Cliff, NJ, 1973.

31. Bowman, J. J.; Senior, T. B. A.; Uslenghi, P. L. E. *Electromagnetic and Acoustic Scattering by Simple Shapes*; Hemisphere: New York, 1987.

32. Lyalinov, M. A. Electromagnetic Scattering by a Circular Impedance Cone: Diffraction Coefficients and Surface Waves. *IMA J. Appl. Math.* **2014**, *79*, 393–430. DOI: 10.1093/imamat/hxs072.

33. Kurihara, K.; Otomo, A.; Syouji, A.; Takahara, J.; Suzuki, K.; Yokoyama, S. Superfocusing Modes of Surface Plasmon Polaritons in Conical Geometry Based on the Quasi-Separation of Variables Approach. *J. Phys. A: Math. Theor.* **2007**, *40*, 12479. DOI: 10.1088/1751-8113/40/41/015.

34. Ashley, J. C.; Emerson, L. C. Dispersion-Relations for Non-Radiative Surface Plasmons on Cylinders. *Surf. Sci.* **1974**, *41*, 615–618. DOI: 10.1016/0039-6028(74)90080-6.

35. Pfeiffer, C. A.; Economou, E. N.; Ngai, K. L. Surface Polaritons in a Circularly Cylindrical Interface - Surface Plasmons. *Phys. Rev. B* **1974**, *10*, 3038–3051. DOI: 10.1103/PhysRevB.10.3038.

36. Novotny, L.; Hafner, C. Light Propagation in a Cylindrical Waveguide With a Complex, Metallic, Dielectric Function. *Phys. Rev. E: Stat. Phys., Plasmas, Fluids, Relat. Interdiscip. Top.* **1994**, *50*, 4094–4106. DOI: 10.1103/PhysRevE.50.4094.

37. Prade, B.; Vinet, J. Y. Guided Optical Waves in Fibers with Negative Dielectric Constant. *J. Lightwave Technol.* **1994**, *12*, 6–18. DOI: 10.1109/50.265728.

38. Issa, N.; Guckenberger, R. Optical Nanofocusing on Tapered Metallic Waveguides. *Plasmonics* **2007**, *2*, 31–37. DOI: 10.1007/s11468-006-9022-7.

39. Talebi, N.; Vogelgesang, R.; van Aken, P. Determining an Electromagnetic Response of a Sample. U.S. Patent US 20140297205 A1, 2014.

40. Talebi, N.; Sigle, W.; Vogelgesang, R.; van Aken, P. Numerical Simulations of Interference Effects in Photon-Assisted Electron Energy-Loss Spectroscopy. *New J. Phys.* **2013**, *15*, 053013. DOI: 10.1088/1367-2630/15/5/053013.

41. Talebi, N. A directional, Ultrafast and Integrated Few-Photon Source Utilizing the Interaction of Electron Beams and Plasmonic Nanoantennas. *New J. Phys.* **2014**, *16*, 053021. DOI: 10.1088/1367-2630/16/5/053021.